Supporting Information for:

Characterization of resistances of a capacitive deionization system

Yatian Qu,[1,2] *Theodore F. Baumann,*[2] *Juan G. Santiago,*[1]* *Michael Stadermann*[2]*

[1] Department of Mechanical Engineering, Stanford University Stanford, CA 94305, USA

[2] Lawrence Livermore National Laboratory, 7000 East Avenue, Livermore, CA, USA.

*To whom correspondence should be addressed. E-mails: juan.santiago@stanford and stadermann2@llnl.gov

This document contains supplementary information and figures further describing our calculation and estimation of resistances in capacitive deionization (CDI) cells; our LTSpice simulations of time-dependent current or voltage responses of CDI systems based on our model; and measured mechanical properties of hierarchical carbon aerogel monoliths (HCAMs).

- S-1: Energy dissipation analysis of a CDI system based on a simple RC circuit model
- S-2: Resistance calculation and estimation in CDI cells
- S-3: Procedures to extract an equivalent series resistance from charging or discharging profiles
- S-4: Internal diagnosis of our CDI cell
- S-5: Time constants in CDI cells
- S-6: LTSpice simulations of time-dependent responses of CDI systems
- S-7: Compression test of HCAM samples
- S-8: Extracted resistance and interfacial capacitance from EIS data for our flow-through CDI cell

Number of pages: 15
Number of figures: 6
Number of tables: 1

S-1: Energy dissipation analysis of a CDI system based on a simple RC circuit model

Perhaps the simplest and yet still somewhat useful model for the energy dissipation of a CDI system is a simple RC circuit: a capacitor in series with a resistor. The capacitor *C* represents the total electrical double layer capacitances for salt removal and the resistor *R* represents an effective total resistance of the cell. To further simply the analysis, we further assume that resistance and capacitance do not change during charging or discharging.

The energy dissipation is different if the cell is run under constant voltage (CV) or constant current (CC) operation. The former is convenient, but that latter can be used to decouple energy use from the speed of desalting. We here discuss both approaches.

For CV operational mode, the current response of an RC circuit is

$$I(t) = \frac{V_{VC}}{R} e^{-t/RC}. \tag{1}$$

Then, the instantaneous dissipation power is

$$P(t) = I(t)^2 R = \frac{{V_{VC}}^2}{R} e^{-2t/RC}. \tag{2}$$

If the cell is charged to finite *t*, then the accumulated dissipated energy is

$$E_{CV}(t) = \int_0^t P(t)dt = \int_0^t \frac{{V_{VC}}^2}{R} e^{-2t/RC} dt = \frac{1}{2} CV^2 (1 - e^{-2t/RC}). \tag{3}$$

The above equation shows that both resistance *R* and charge time *t* of CDI (e.g., in minutes) are important operational metrics of CDI cells.

We note that if a CDI cell is charged to infinite time, the energy consumption is $CV^2/2$. However, in practical applications, we cannot and would not want to charge a CDI cell for very long times (e.g., until current is reduced to less than 20% of its maximum) as this leads to very slow salt removal rate. For finite charging time, the RC circuit response is a

strong function of both resistance R and charging time t.

For CC operational mode, the RC circuit dissipated energy is simply:

$$E_{CC}(t) = I_0^{\,2} R t \ . \tag{4}$$

Here, I_o is the constant current. Resistance R is obviously a key parameter.

Interestingly, if we charge a cell at CC mode for a time such that the charge transferred is the same as that transferred in CV mode, we can derive:

$$I_0 = \frac{1}{t_{CC'}} \int_0^{t_{CC'}} \frac{V'}{R} e^{-t/RC}\, dt = \frac{V'C}{t_{CC'}} (1 - e^{-t_{CC'}/RC}) \ , \tag{5}$$

Here the subscript CC' refers to charging at constant current until accumulated charge is equal to the steady state charge of constant voltage charging at voltage V'. Voltage of a CDI cell V varies in time for all CC but V' is the constant value associated with CV mode.

$$E_{CC'} = \int_0^{t_{CC'}} P\, dt = \int_0^{t_{CC'}} I_0^2 R\, dt = I_0^2 R \int_0^{t_{CC'}} dt = I_0^2 R t_{CC'} \tag{6}$$

Combining equation (5) and equation (6), we can derive

$$E_{CC'} = \frac{V'^2 C^2 R}{t_{CC'}} (1 - e^{-t_{CC'}/RC})^2 \ , \tag{7}$$

This energy consumption is again a strong function of resistance R. Therefore, energy consumption for either CV or CC operation mode strongly depends on the effective resistance R.

S-2 Resistance calculation and estimation in CDI cells

Estimation of setup resistance:

Setup resistance includes ionic resistance in separator, electrical resistance of current collectors and connecting wires, as shown in equation (8):

$$R_s = R_{separator} + R_{collector} + R_{wire}\ , \tag{8}$$

Connecting wire resistances can be approximately measured by a multimeter. They usually account for fractions of 1 ohm. In our resistance estimates of CDI devices reported in literature, we assume wire resistance to be 0.3 Ω in all cases.

To estimate the ionic resistance in separator, we use the model described by equation (9) of the main text which we repeat here:

$$R_{separator} = \frac{\tau_s l_s}{\sigma_i \psi_s A_s}, \tag{9}$$

Here, l_s is the thickness of separator, A_s is the geometric cross-section area of separator, σ_i is the conductivity of salt solution, Ψ_s is the porosity of the separator, and τ_s represents the tortuosity of the separator.

For current collector resistance, we calculate it using equation (10):

$$R_{collector} = \frac{l_c}{\sigma_c A_c}, \tag{10}$$

l_c is the thickness of current collector, A_c is the geometric cross-section area of current collector, and σ_c is the electrical conductivity of current collector.

Estimation of ionic resistance across an ion exchange membrane

For a CDI cell with one or more ion exchange membranes, we include the ionic resistance across the membrane when estimating the total characteristic series resistance. This resistance can be calculated using the information reported in the product specification sheets of the membranes, which is usually reported in the form of sheet resistance of the membrane when filled with a specified concentration of test solution. These test solutions are often chosen by membrane manufacturers to minimize the reported resistance. Hence, we typically assume this reported resistance as a minimum expected resistance of the membrane, and independent of feed water concentration.

Estimation of the nominal value of solution ionic resistance (for the solution inside porous electrodes):

For the purpose of resistance estimations, we model porous electrodes simply as a large number of idealized and non-intersecting, tortuous microchannels in parallel[1] (Figure S-1). This structure can be characterized by the total volume of electrodes, V_e, the void volume, V_v, its macroscopic thickness l_e, and the tortuous characteristic length of the pores L_e. The ratios V_v / V_e and L_e / l_e are defined as the porosity Ψ_e and tortuosity τ_e, respectively. Given this, the nominal ionic resistance of salt solution in porous electrode is given by eq. (11):

$$R_i = \frac{\tau_e l_e}{\sigma_i \psi_e A_e}, \tag{11}$$

Here A_e is the geometric cross-section area of an electrode, σ_i is the conductivity of salt solution. As discussed in main text, we used typically reported tortuosity and porosity numbers for activated carbon and carbon aerogel materials: $\tau_e = 3.5$[2,3] ; $\psi_e = 0.8$.

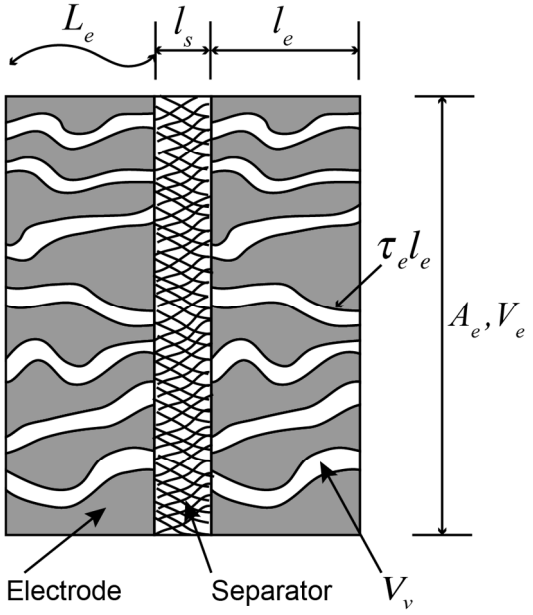

Figure S-1. Schematic of the model of porous electrode and separator of a CDI cell.

S-3 Procedures to extract an area-normalized equivalent series resistance (ANESR) from charging or discharging profiles

As described in the main paper, we define area-normalized equivalent series resistance (ANESR) in each of two operational modes: constant current (CC) and constant voltage (CV). Within each mode, we also define charging resistances and discharging ANESR. Figure S-2a illustrates charging and discharging absolute equivalent series resistances (ESRs) in a simulated CC cycling profile; and Figure S-2b describes these two ESRs in a simulated CV cycling profile. The associated simulations are described in more detail in Section S-6 below. As per our resistance model, this ESR is approximately the sum of setup resistance and contact resistance: $R_s + R_{ct}$. We then normalize ESR by electrode geometric area A and cell number in a stack N to obtain ANESR, $(R_s + R_{ct})AN$.

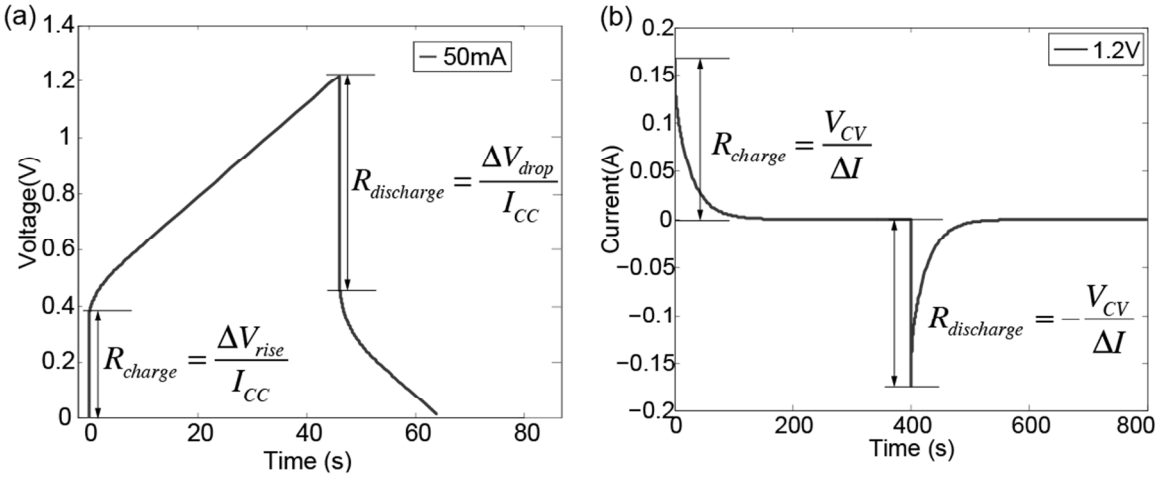

Figure S-2. ESRs in charging and discharging cycling profiles in one of two operational modes: a) CC operation mode; b) CV operation mode. Shown are simulations of a CDI cell using the model discussed in Section S-6 below.

S-4 Internal diagnosis of our CDI cell

Figure S-3a shows a typical measured charging profile of our flow-through CDI cell in CV mode at 1 V. We divide the voltage by instant charging current to obtain a charging ESR as 60.9 Ω. This resistance is much larger than the setup resistance (0.5 Ω) as we estimated from solution and separator properties. To diagnose the components of the measured ESR, we performed EIS to the whole cell, as shown in Figure S-3b. The extracted value of this contact resistance is 57.2 Ω, which constitutes 94% of ESR in our cell. This observation supports the hypothesis that contact resistance is the major contributor to internal resistance in CDI cells.

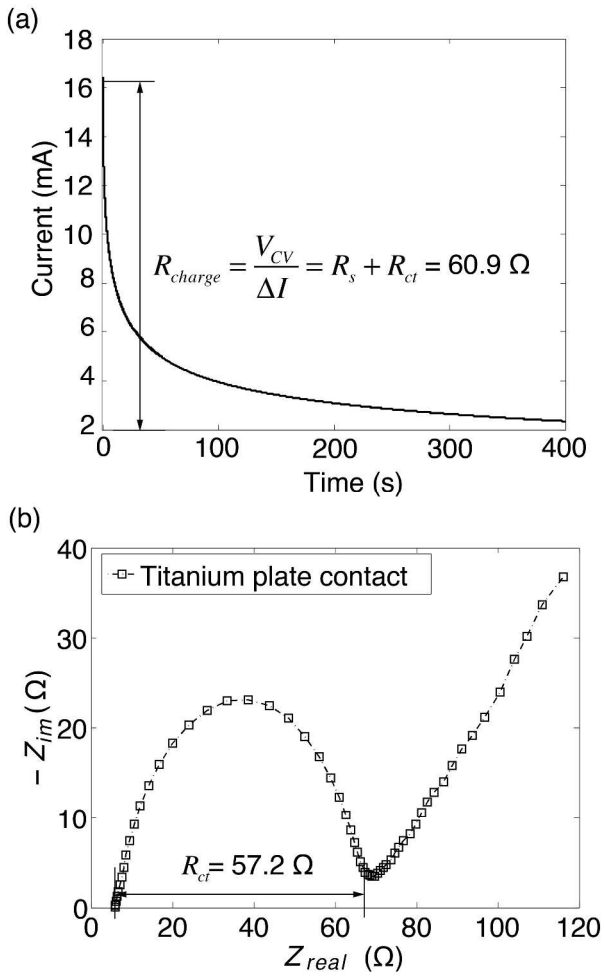

Figure S-3. (a) ESR extraction from CV charging profile of our flow-through CDI cell. The extracted ESR is 60.9 Ω; (b) Nyquist plot of flow-through CDI cell with 100 mM NaCl. The contact resistance extracted from this EIS data is 57.2 Ω, indicating the majority of ESR is contact resistance.

S-5 Time constants in CDI cells

As per the equivalent circuit model we propose in the main paper (Figure 1b), there are two time constants associated with the charging and discharging dynamics of a CDI cell. The first time constant, τ_{RC}, is for the contact resistance and interfacial capacitance pair. This can be estimated by equation (12):

$$\tau_{RC} = R_{ct} C_{ct} \tag{12}$$

In our CDI cell, R_{ct} is measured 7 Ω and C_{ct} is approximately 20 μF. So τ_{RC1} is estimated to be on the order of a hundred microseconds. This means that when charging starts, the contact resistance and interfacial capacitor parallel pair quickly transit to an equilibrium state. When performing either CC or CV cycling, the first data point is usually recorded after a few milliseconds due to the delay associated with the response time of the most experimental equipment. Therefore, this very quick transition is usually missed by instruments used in CDI experiments.

The second time constant (τ_{RC2}) is the transmission line (TL) time constant. This time constant is approximately the multiplication of half of the nominal ionic resistance and the electrical double layer capacitance of each porous electrode,[4,5] as described by equation (13):

$$\tau_{RC2} = \frac{1}{2} R_i C_i = \frac{\tau_e l_e}{2\sigma_i \psi_e A_e} C_i, \tag{13}$$

In our cell, half of R_i is 5.1 Ω and C_i is 6 F per electrode. Therefore, the time constant of the TL is 30.6 s.

S-6: LTSpice simulations of time-dependent responses of CDI systems

We performed LTSpice simulations to explore the charging/discharging dynamics of a CDI cell. In our model, we have a setup resistance, a pair of contact resistances and interfacial capacitance in parallel, and two electrodes each modeled via a TL with 20 resistor-capacitor units (Figure S-4). Each resistor or capacitor unit has a value that was chosen to reflect the actual resistances or capacitances in our flow-through CDI cell. We estimated R_s and R_i as described in Section S-2. We estimated R_{ct} by subtracting R_{ct} from the ESR (R_s + R_{ct}) measured in a CV cycling profile. The estimated R_i and R_e of each electrode are related to the resistance of each element R_{i1}, R_{i2}, ...R_{i19} and R_{e1}, R_{e2}, ...R_{e20} as follows:

$$R_{i(j)} = R_i/N_i, \;\; R_{e(k)} = R_e/N_e \quad (j=1,2, ..., 19; \; k=1,2, ..., 20) \tag{14}$$

where N_i and N_e are the (arbitrarily chosen) number of elements of our discretization. We here chose N_i as 19 and N_e as 20 for each electrode.

To measure capacitance of each electrode C_i, we performed cyclic voltammetry of the whole CDI cell. The capacitance of each electrode C_i is related to each capacitor in the circuit $C_{i1}, C_{i2}, \ldots C_{i20}$ as follows:

$$C_{i(m)} = C_i/N_c, (m=1,2, ..., 20) \quad (15)$$

we here chose N_c as 20.

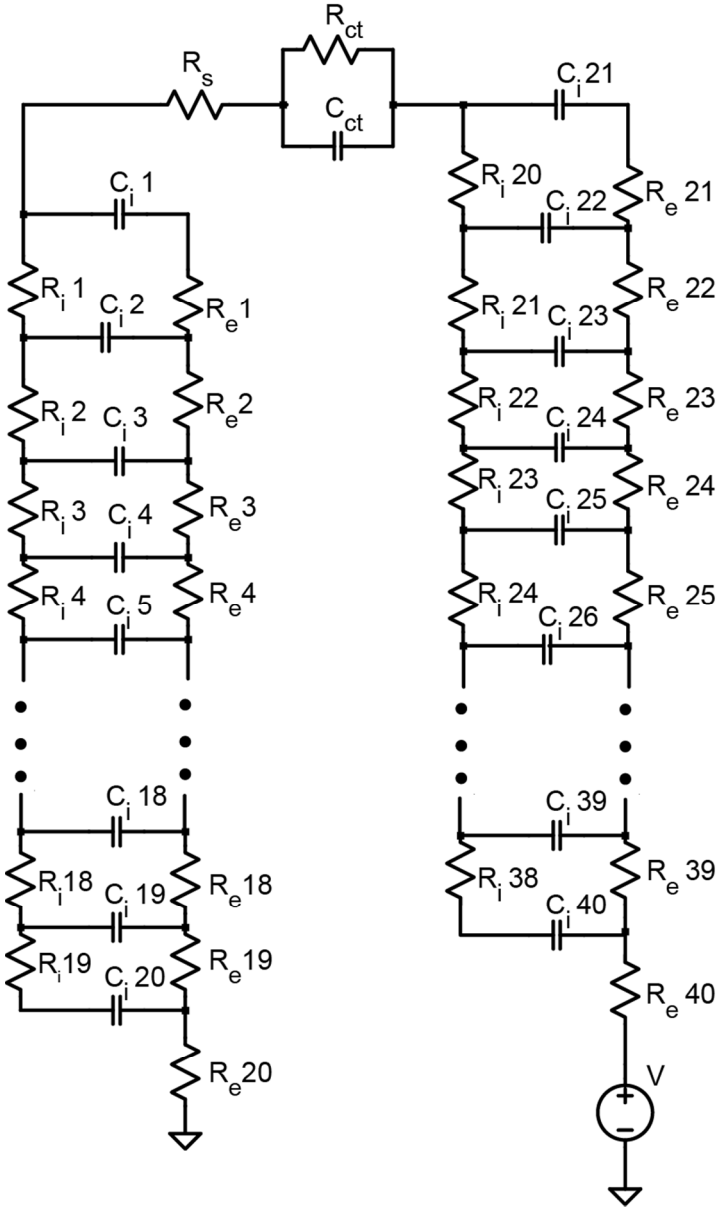

Figure S-4. Schematic of equivalent circuit model used in our LTSpice simulation. We discretized the electrodes using a simple transmission line modeling approach. The values of each resistor and capacitor element were chosen to correctly reflect the total resistance and capacitance of our cell from experiments.

We simulated charging and discharging cycles in both CV and CC operation modes. The current and voltage responses depend on the time regimes of the simulation. Figure S-5a shows the current response in CV mode with 1.2 V charging voltage within 100 μs after the cycle starts. The model exhibits a relatively high and sharp current spike within this time regime due to the rapid charging of the interfacial capacitor C_{ct}, as expected. As mentioned above, we hypothesize that this high current spike is not typically observed in practice due to the common limitations of experimental setups. For example, potentiostats limit the maximum current that can be drawn in the system to protect their circuitry. In addition, data recorded by potentiostats usually has a time delay due to the experiment configuration and instrument limitation. This time delay is usually on the order of several milliseconds. For example, in the experiments presented in this work, this time delay is approximately 10 ms.

Figure S-5b shows the current response from more easily addressable regime of 10 ms to 50 s under the same charging condition. This plot is more representative of current responses observed in CV cycling experiments. Plotted in S-5c is the value of current as a function of resistor number in the abscissa and time in the ordinate. The dark lines are contours separated at an increment of 17 mA. The contour shapes demonstrate the propagation current flow from high to low values of the bulk material electrical resistor number (R_{ek}) and from low to high values of the ionic resistors number (R_{ij}) immediately after applying 1.2 V constant voltage at t = 0 s. The applied voltage is reversed at t = 400 s, and again we see discharging current propagating from high to low numbers of R_{ek} and from low to high numbers of R_{ij}. These contours show how the system quickly achieves mirror symmetry of the current distribution through ionic resistors vs. the current distribution through bulk material electrical conductive resistors. Since the bulk material conductive resistance R_e is negligible (only 0.0065 Ω per electrode in our model), in the fully developed charging state (where the current is approximately evenly distributed between bulk electrode resistance R_e and the solution ionic resistance in porous electrode R_i), the equivalent resistance of a porous electrode is then approximated as $R_i/2$.

Figure S-5d shows the voltage response in CC mode with 1 mA charging current within 100 μs after the cycle starts. The nearly instantaneous voltage rise at the beginning is only associated with the setup resistance R_s. Figure S-5e shows the voltage response from 10 ms to 50 s under the same charging condition. As discussed in Section S-5, the time constant associated with the product of R_{ct} and C_{ct} is on the order of a hundred microseconds. Therefore, in this time regime, the interfacial capacitor C_{ct} is saturated and the mainstream current only passes through R_{ct}. The voltage rise at the beginning in Figure S-5e is then associated with the sum of setup resistance R_s and contact resistance R_{ct}, which is the ESR we have defined for charging/discharging cycles. Plotted in S-5f is the value of current as a function of resistor number in abscissa and time in the ordinate. Here, the dark lines are contours separated at an increment of 7.4 mA. The contours demonstrate the propagation current flow from high to low values of the bulk material electrical resistor number (R_{ek}) and from low to high values of the ionic resistors number (R_{ij}) immediately after applying 50 mA constant current at t = 0 s. The applied current is reversed at t = 46 s, and again we see discharging current propagating from high to low numbers of R_{ek} and from low to high numbers of R_{ij}. Similar to CV mode, these contours also show how the system achieves mirror symmetry of the current distribution between ionic resistors vs. bulk material electrical conductive resistors at fully developed charging state. Therefore, at fully developed charging state (where the current is approximately evenly distributed between bulk electrode resistance R_e and the solution ionic resistance in porous electrode R_i), the equivalent resistance of a porous electrode is also $R_i/2$.

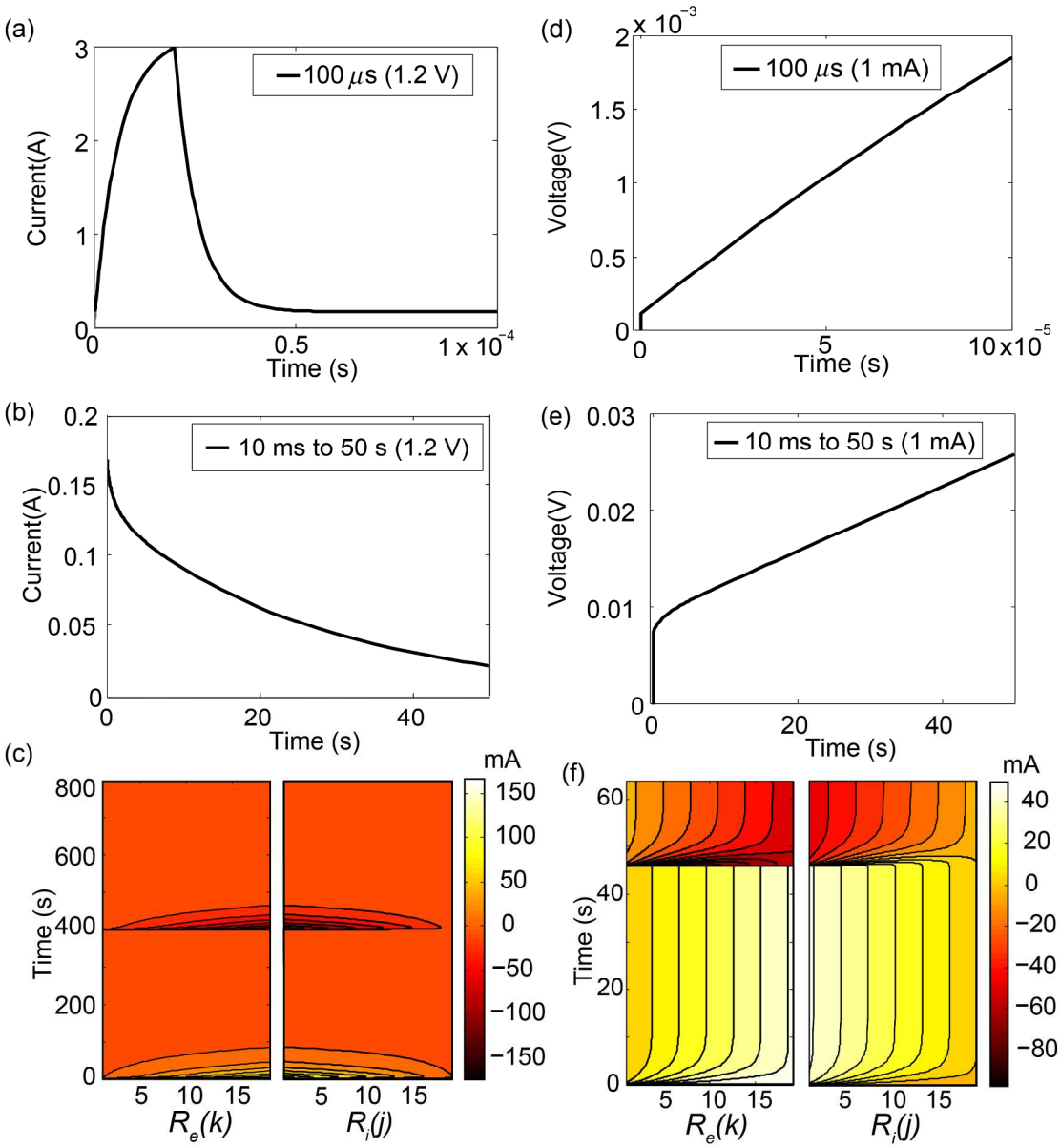

Figure S-5. Current and voltage responses for a CDI cell operated in CV and CC modes. (a) – (c) show current responses of a CDI cell in CV mode with 1.2 V in (a) 100 μs and (b) 10 ms to 50 s charging regime, (c) shows the mirror symmetry of current distribution through the bulk material electrical resistors $R_e(k)$ and ionic resistors $R_i(j)$ at fully developed charging state in a CV cycle with 1.2 V charging voltage. (d) – (f) show voltage responses of a CDI cell in CC mode with 1 mA in (d) 100 μs and (e) 10 ms - 50 s charging regimes, (f) shows the mirror symmetry, at fully developed charging state, of current distribution through the bulk material electrical resistors $R_e(k)$ and ionic resistors $R_i(j)$ in a CC cycle with 50 mA charging/discharging current.

S-7: Compression test of HCAM samples

We performed nanoindentation of HCAM material to evaluate its elastic modulus. HCAM samples were tested in a homebuilt machine that was designed specially for ultralow-stiffness materials.[6,7] The indentation was performed with a steel sphere indenter with the radius of 1mm at displacement speed of 50 μm/min. Figure S-6 shows the typical loading and unloading curves of HCAM samples. The inset figure shows the unloading Young's modulus obtained from analyzing load-unload data. The loading might include inelastic deformation, whereas unloading is purely elastic bouncing. Consequently, we here use the unloading Young's modulus as our estimate of the elastic modulus of HCAM material. The measured elastic modulus of the HCAM samples is within the range from 110 to 137 MPa. These data further support our conclusion that our compression experiments described in the main paper are within the elastic response region for the HCAM.

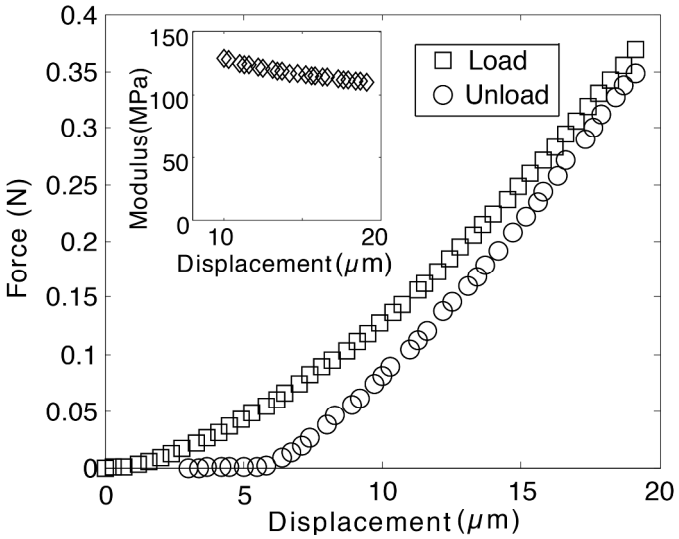

Figure S-6. Typical continuous load-unload curves for a HCAM sample indented with steel sphere indenter. Inset shows the unloading Young's modulus obtained from load-unload data analysis.

S-8: Extracted resistance and interfacial capacitance from EIS data for our flow-through CDI cell

We extracted numbers of resistance and interfacial capacitance from the EIS data shown in Figure 4 of the main paper, using the equivalent circuit proposed in Figure 1b in the main paper. We converted constant phase element parameter Q_{ct} to interfacial capacitance C_{ct}.[8] Table S-1 summarizes the extracted resistance and interfacial capacitance. As pressure increased from less than 1 to 30 kPa, the dominant semicircle feature of the Nyquist plot shrunk. The contact resistance, which is associated with the diameter of semicircle feature, decreased from 8.8 to 5.5 Ω, nearly 40% reduction. At the same time, the interfacial capacitance was reduced by 7.7% from 22.0 μF to 20.3 μF. The capacitance did not change substantially, but appeared to trend downward with increased pressure. These trends indicate that contact area was created at the expense of reducing the capacitive surface, and that the sum of the microscopic electrical contact area and interfacial capacitance surface area was not constant.

Table S-1 Extracted resistance and interfacial capacitance from EIS data for our flow-through CDI cell

Pressure (kPa)	R_s (Ω)	C_{ct} (μF)	% of C_{ct} reduced	R_{ct} (Ω)	% of R_{ct} reduced
<1	0.58	22.0	0%	7.5	0%
5	0.56	21.5	2.2%	6.8	9.3%
15	0.58	20.9	5.0%	5.8	23%
30	0.63	20.3	7.7%	4.8	36%

REFERENCES

1. Yao, S.; Santiago, J. G. Porous glass electroosmotic pumps: theory. *J. Colloid Interface Sci.* **2003,** *268*, 133-142.

2. Jayne, D.; Zhang, Y.; Haji, S.; Erkey, C. Dynamics of removal of organosulfur compounds from diesel by adsorption on carbon aerogels for fuel cell applications. *Int. J. Hydrogen Energy* **2005,** *30*, 1287-1293.

3. Leyva-Ramos, R.; Geankoplis, C. J. Diffusion in liquid-filled pores of activated carbon. I. Pore volume diffusion. *Can. J. Chem. Eng.* **1994,** *72*, 262-271.

4. Biesheuvel, P. M.; Bazant, M. Z. Nonlinear dynamics of capacitive charging and desalination by porous electrodes. *Physical Review E* **2010,** *81*, 031502(1-12).

5. Suss, M. Capacitive water desalination with hierarchical porous electrodes. Ph.D. Dissertation, Stanford University, Stanford, CA, 2013.

6. Kucheyev, S. O.; Hamza, A. V.; Satcher Jr, J. H.; Worsley, M. A. Depth-sensing indentation of low-density brittle nanoporous solids. *Acta Mater.* **2009,** *57*, (12), 3472-3480.

7. Kucheyev, S. O.; Stadermann, M.; Shin, S. J.; Satcher, J. H., Jr.; Gammon, S. A.; Letts, S. A.; van Buuren, T.; Hamza, A. V. Super-compressibility of ultralow-density nanoporous silica. *Adv. Mater.* **2012,** *24*, (6), 776-780.

8. Hsu, C. H.; Mansfeld, F. Technical note: concerning the conversion of the constant phase element parameter Y_0 into a capacitance. *Corrosion* **2001,** *57*, (9), 747-748.